Nanoscale Characterization of Back Surfaces and Interfaces in Thin-Film Kesterite Solar Cells

Kasra Sardashti,[†,‡] Evgueni Chagarov,[†] Priscilla D. Antunez,[§] Talia S. Gershon,[§] Scott T. Ueda,[†] Tayfun Gokmen,[§] Douglas Bishop,[§] Richard Haight,[§] and Andrew C. Kummel*,[†]

[†]Department of Chemistry and Biochemistry and [‡]Materials Science and Engineering Program, University of California, San Diego, 9500 Gilman Drive, La Jolla, California 92093, United States
[§]IBM T. J. Watson Research Center, 1101 Kitchawan Road, Yorktown Heights, New York 10598, United States

Ⓢ *Supporting Information*
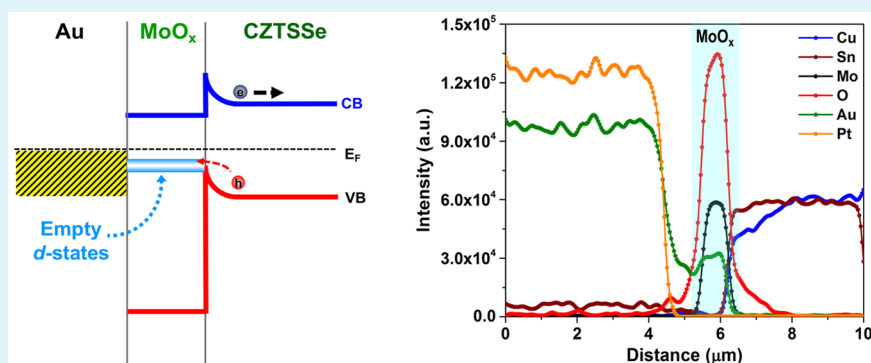
ABSTRACT: Combinations of sub 1 μm absorber films with high-work-function back surface contact layers are expected to induce large enough internal fields to overcome adverse effects of bulk defects on thin-film photovoltaic performance, particularly in earth-abundant kesterites. However, there are numerous experimental challenges involving back surface engineering, which includes exfoliation, thinning, and contact layer optimization. In the present study, a unique combination of nanocharacterization tools, including nano-Auger, Kelvin probe force microscopy (KPFM), and cryogenic focused ion beam measurements, are employed to gauge the possibility of surface potential modification in the absorber back surface via direct deposition of high-work-function metal oxides on exfoliated surfaces. Nano-Auger measurements showed large compositional nonuniformities on the exfoliated surfaces, which can be minimized by a brief bromine−methanol etching step. Cross-sectional nano-Auger and KPFM measurements on Au/MoO$_3$/Cu$_2$ZnSn(S,Se)$_4$ (CZTSSe) showed an upward band bending as large as 400 meV within the CZTSSe layer, consistent with the high work function of MoO$_3$, despite Au incorporation into the oxide layer. Density functional theory simulations of the atomic structure for bulk amorphous MoO$_3$ demonstrated the presence of large voids within MoO$_3$ enabling Au in-diffusion. With a less diffusive metal electrode such as Pt or Pd, upward band bending beyond this level is expected to be achieved.

KEYWORDS: thin-film photovoltaics, back contacts, CZTSSe, cryo-FIB, KPFM, nano-Auger

■ INTRODUCTION

While photovoltaics (PV) is one of the leading technologies for generation of renewable energy, it only contributes to ∼1% of global electricity production.[1] For PV to be a major source of electricity, lower cost per watt of generated power, particularly through reduction in the module production cost, is essential.[2] This cost reduction goal has stimulated development of thin-film PV technologies that employ thin layers (thickness <5 μm) of direct-band-gap absorbers compatible with large-area monolithic integration.[3,4] The two leading thin-film PV technologies based on Cu(In,Ga)Se$_2$ (CIGSe) and CdTe absorbers have achieved cell efficiencies as high as 22%.[5,6] However, their dependence on relatively scarce (i.e., In, Ga, and Te) or toxic (i.e., Cd) elements could impose potential

limitations on the sustainable large-scale deployment of these technologies.[4,7]

Kesterite Cu$_2$ZnSn(S,Se)$_4$ (CZTSSe) absorbers are the most promising nontoxic and earth-abundant alternatives to CIGSe and CdTe. However, the CZTSSe record efficiency is about 12.6%; there is an almost 10% gap in efficiency between CZTSSe and CIGSe.[8] This performance gap has been mainly attributed to the large density of bulk defects in CZTSSe, particularly Cu−Zn antisite defects.[9−16] One potential approach to overcome the large bulk defect density is to use thinner absorbers in combination with high-work-function
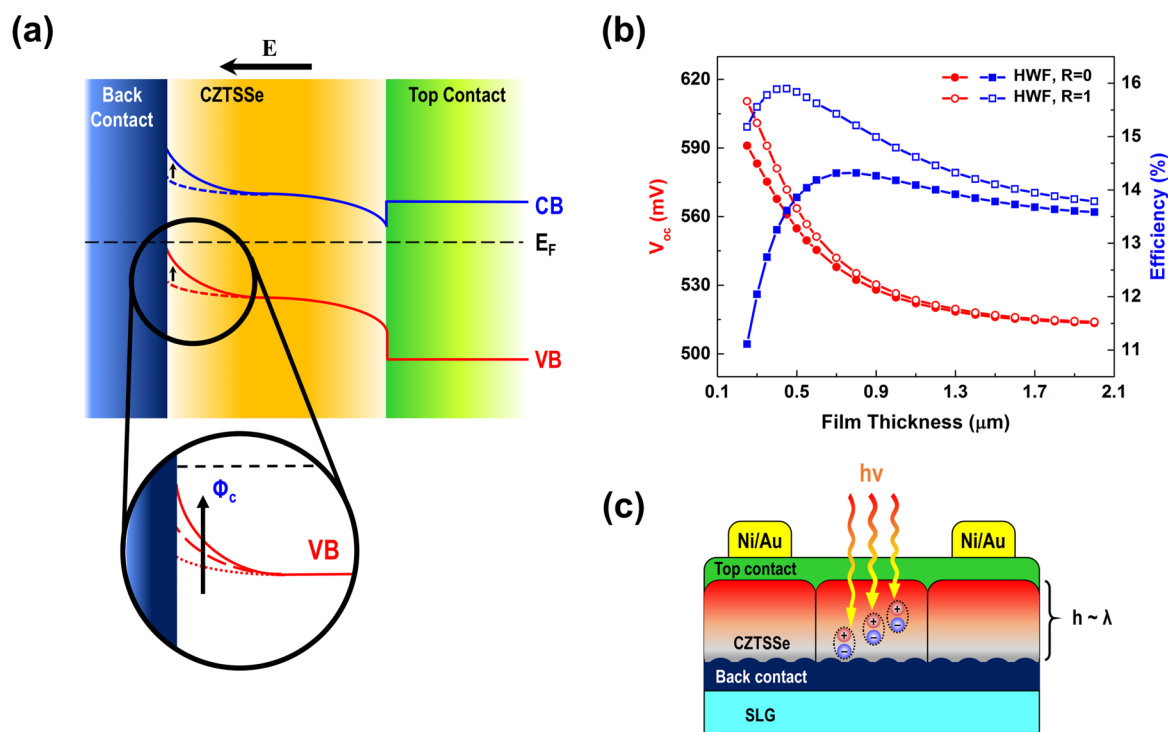
Figure 1. Combination of high-work-function back contacts and thinner absorbers: (a) band alignment within a sub 1 μm thin-film solar cell with the effect of the higher back contact work function shown as solid lines in the diagram; (b) V_{OC} and power conversion efficiency as functions of the kesterite absorber film thickness, simulated by wxAMPS for highly reflective ($R = 1$) and nonreflective ($R = 0$) back contacts; (c) schematic showing the exciton formation region in thinner absorber films, which is close to the back surface and contact/absorber interfaces.

contact materials to increase the internal electric field (Figure 1a).[17,18] Although application of high-work-function back contact layers such as MoO_x to thick CIGSe and CdTe devices have led to improvements in performance by reducing the interface barrier, due to the larger density of bulk defects in CZTSSe, significant improvements in performance can only be expected in combination with films thinner than 1.5 μm.[19,20] Therefore, as shown in Figure 1b, only for sub 1 μm films with highly reflective large-work-function contacts power conversion efficiencies beyond 15% are expected.

Sub 1 μm films can be grown directly onto high-work-function buffers, or thicker films can be exfoliated and thinned followed by buffer deposition.[21,22] While high-work-function materials such as MoO_3,[23] WO_3,[24] etc. could be directly deposited by physical vapor deposition on various surfaces, their limited chemical and thermal stabilities necessitate major modifications to the film growth conditions to ensure their successful integration into the film growth processes.[25,26] Therefore, exfoliation of thick films, followed by etching and contact deposition, could be a more practical alternative in realizing thin devices combined with high-work-function contact layers. While exfoliation processes have not been extensively discussed for CZTSSe/Mo/glass stacks, mechanical exfoliation has been previously achieved for CIGSe utilizing CIGSe/$MoSe_2$ interfaces, which is attributed to the weak van der Waals forces between $MoSe_2$ layers.[27,28] Although exfoliations of CIGSe films were mostly performed with the purpose of transferring high-quality devices onto flexible substrates, a few reports also focused on compositional analysis of the back surface via X-ray photoelectron spectroscopy (XPS)), confirming that the exfoliation occurs at the $MoSe_2$/Mo interfaces.[27,29,30]

As shown schematically in Figure 1c, once the kesterite film becomes thinner than ~1 μm, the photon absorption length (λ) is comparable to the film thickness (h).[31,32] This results in a larger number of interactions between the back surface defects and photogenerated carriers. As a result, the composition and defect structure of the back surface and kesterite/contact interfaces could play a more significant role in the overall carrier recombination. Therefore, it is necessary to characterize the kesterite back surface composition and electronic structure after the exfoliation and chemical etching processes.

In the present study, nanocharacterization tools, including nano-Auger, Kelvin probe force microscopy (KPFM), and cryogenic focused ion beam (cryo-FIB), are employed to determine the influence of processing steps, including exfoliation, etching, and MoO_3 deposition on the electronics and chemistry of the back surfaces/interfaces in CZTSSe thin-film solar cells. CZTSSe films were mechanically exfoliated along the CZTSSe/Mo(S,Se)$_2$ interfaces and thinned by chemical etching (via bromine−methanol solution) and chemical-mechanical polishing (CMP). Note that thinning was limited to 200 nm due to pinhole formation. The compositions of the back surfaces before and after the etching were evaluated by nano-Auger elemental analysis. Smooth cross-sections for cross-sectional nano-Auger and KPFM measurements were prepared by grazing angle of incidence cryo-FIB.[33,34] Cross-sectional KPFM measurements revealed that MoO_3 as a hole transport layer induces larger upward band bending in CZTSSe in comparison with Mo(S,Se)$_2$. However, Au diffusion into MoO_3 resulted in work function and potential fill factor degradation. Density functional theory (DFT) simulations demonstrated that the large void density in amorphous MoO_3 is consistent with Au in-diffusion. A further increase in back surface band bending is expected by exploring
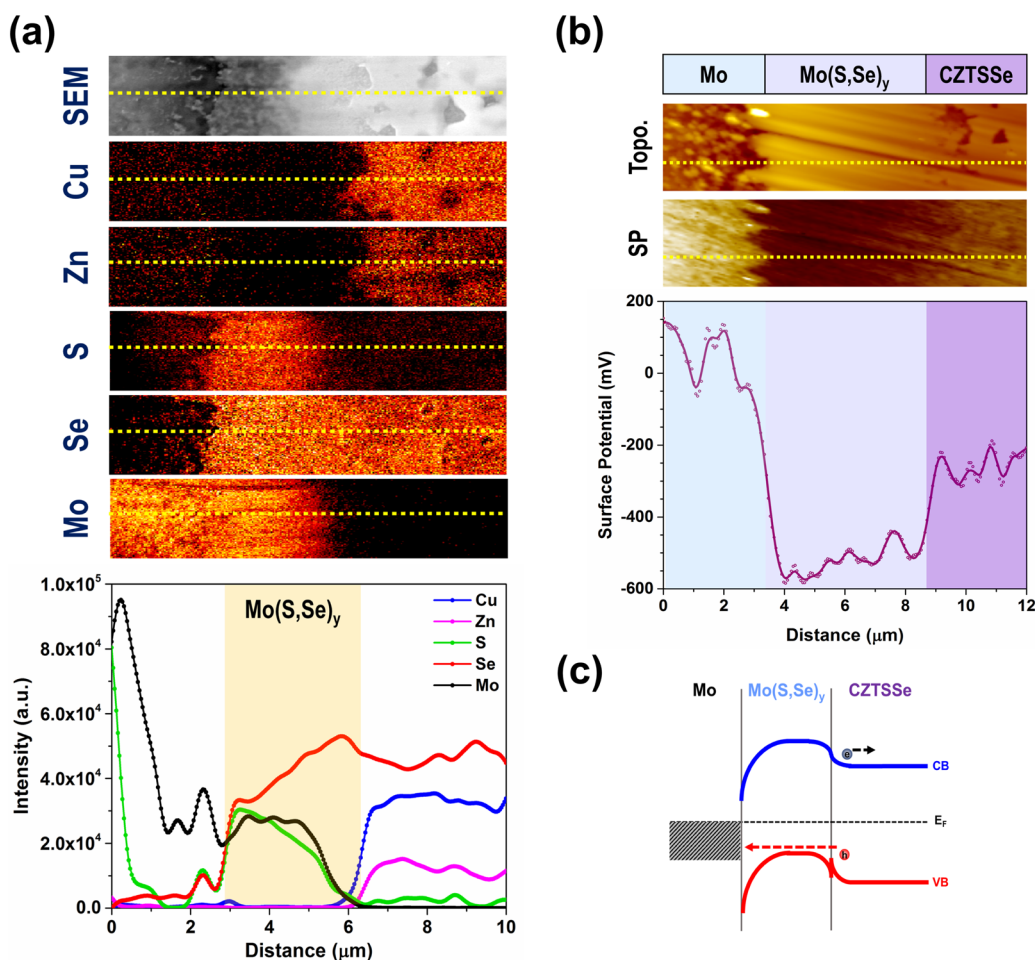
Figure 2. Cross-sectional nano-Auger and KPFM measurements for the CZTSSe/Mo interface: (a) SEM micrograph and elemental maps measured by nano-Auger on a CZTSSe/Mo sloped cross-section (a line scan (dotted line) measured for Cu, Zn, S, Se, and Mo is shown at the bottom); (b) topography and surface potential (SP) maps measured by KPFM on the sloped cross-sections (a line scan (dotted line) extracted from the SP measurements is shown at the bottom); (c) estimated band diagram at the back interface derived from the measured work function values beside band edge positions reported in the literature.[50−52] Cross-sections were prepared by grazing angle of incidence cryo-FIB with 5−8° angles of incidence.

alternative contact layers and metal electrodes with a smaller tendency for interdiffusion or intermixing.

■ EXPERIMENTAL SECTION

Film Growth, Exfoliation, and Solar Cell Fabrication. CZTSSe thin films were grown by the IBM hybrid solution−particle method. Details of the growth method are described elsewhere.[8,35,36] CZTSSe films were grown on Mo-coated soda lime glass (SLG). After being spin coated onto the Mo/SLG substrates, the films underwent annealing at 600 °C for 2 min under a N$_2$ atmosphere. To maintain composition and band gap uniformity across the films, no excess S or Se was incorporated during this annealing step. Instead, the S and Se were included in the slurry, and during the N$_2$ anneal, the samples were encapsulated in a glass enclosure to ensure that there is no significant loss of S or Se. Following the N$_2$ anneal, the samples were annealed in air at 300 °C for 10 min, primarily to passivate the grain boundaries. These annealing conditions were optimized for solution-grown CZTSSe solar cells to achieve efficiencies as high as 12.6% as explained in refs 8 and 18. Afterwards, full devices were fabricated by deposition of a CdS buffer layer using chemical bath deposition followed by radio frequency (rf) magnetron sputtering of a ZnO window and an indium tin oxide (ITO) top transport layer. The devices were completed by the deposition of 2 μm thick Ni/Al collector grids on top of the ITO layer. Full devices were then attached to a fused silica carrier using an epoxy. Mechanical exfoliation was achieved by a sudden impact laterally applied to the CZTSSe/Mo rear interface using a chisel (Supporting Information, Figure S1).

To reduce the thickness, the exfoliated films underwent chemical etching in 0.125 M bromine−methanol (Br−Me) for 15−45 s. Alternatively, exfoliated films were treated with 10 min of chemical-mechanical polishing (CMP) using a polish slurry composed of dilute HCl solutions and Al$_2$O$_3$ particles (further details of the CMP process are given in the Supporting Information). Profilometry measurements showed up to 200 nm reduction in thickness of the exfoliated films by both these etching methods.

Due to higher compositional uniformity, only films that were treated by 45 s of Br−Me etching were used for high-work-function electrode deposition. For cross-sectional studies, 40 nm MoO$_3$ and 200 nm Au blankets were deposited onto the etched surfaces. For current−voltage (J−V) characterization, solar cells were fabricated by thermal evaporation of ∼20 nm MoO$_3$ blankets and ∼100 nm of Au in the form of circular pads with 2 mm diameter.

J−V Characterization of Solar Cells. PV performance before and after exfoliation was evaluated by J−V measurements using a Newport solar simulator with simulated AM1.5G illumination. A Keithley 2400 sourcemeter was used for bias application and current measurement. Performance parameters such as open-circuit voltage (V_{oc}), short-circuit current (J_{sc}), fill factor (FF), and power conversion efficiency (PCE) were derived directly from the J−V curves. J−V characteristics were measured for the same CZTSSe thin films in pre-exfoliated and

exfoliated (mechanical exfoliation followed by Br−Me and MoO_3/Au deposition) conditions.

Preparation of Cross-Sections. To prepare smooth cross-sections, cryogenic focused ion beam (cryo-FIB; FEI Scios DualBeam) milling at temperatures below 100 K was employed. To expand the thickness scale for each layer by 8−12-fold, grazing angles of incidence (~4−8°) were employed. For Au/MoO_3/CZTSSe stacks, a sacrificial layer of Pt/Ti or Pt/Ti/Si was deposited by direct current (dc)/rf magnetron sputtering. A schematic of the milling process is shown in Figure S2, Supporting Information. Further details of the cryo-FIB cross-sectioning process can be found in refs 33 and 34. Due to the geometry of the grazing angle of incidence milling process, Ga^+ incorporation is expected to occur at the bottom of the milling ramp, which includes the soda lime glass substrate. Single-point nano-Auger spectroscopy performed on the cross-sections confirmed the absence of Ga within the layers of interest within the stack including CZTSSe and Mo(S,Se)$_2$ (Figure S3, Supporting Information). Any Ga^+ incorporation below the nano-Auger detection limits is expected to be limited to depths of a few angstroms from the surface. Due to the short air exposure prior to KPFM analysis, this Ga^+ is expected to be in the thin surface oxide covering the ramp. The carriers that are responding to the local electrical field of KPFM would tunnel through this layer. Therefore, Ga^+ is not expected to make a significant difference in the present KPFM measurements.[37,38]

Kelvin Probe Force Microscopy (KPFM). KPFM measurements were performed using a Keysight 5500 scanning probe microscope with the capability of performing simultaneous topography and surface potential measurements via a dual lock-in amplifier setup.[38] To prevent surface reactions during the measurements, all experiments were performed in an environmental chamber that is constantly purged with an inert gas (i.e., ultra-high-purity N_2 or Ar). All the measurements were performed using highly conductive Pt-coated atomic force microscopy (AFM) probes (NanoSensors PPP).

Auger Nanoprobe Microscopy (Nano-Auger). High-resolution Auger elemental mapping was achieved by using a PHI-700 nano-Auger microscope with a lateral resolution of ∼8 nm. An electron beam of 20 kV, 10 nA, generated by a field emission (FE) electron gun, was focused on the sample surface, and the resulting Auger electrons with various kinetic energies were collected by a cylindrical mirror analyzer (CMA) with a 360° collection angle.[39] Additionally, to remove carbonaceous surface contaminants, the tool is equipped with an Ar^+ ion sputtering gun, which enables low-energy in situ Ar^+ sputtering prior to elemental analysis.

Density Functional Theory (DFT) Modeling. All DFT simulations were performed with the Vienna Ab initio Simulation Package (VASP) using projector augmented wave (PAW) pseudopotentials (PPs) and the Perdew−Burke−Ernzerhof (PBE) exchange-correlation functional.[40−45] Since standard DFT functionals such as PBE underestimate the band gap, the electronic structure at the final stage was calculated with the more accurate HSE06 hybrid functional.[46] The systems after relaxation with the PBE functional were rescaled to the HSE06 CZTS$_{0.25}$Se$_{0.75}$ lattice constant different by several percentages. The layers of MoO_x were added in two steps (four plus four MoO_3 molecules). After each deposition, the system was annealed at 400 K for 1000 fs, cooled to 0 K for 200 fs, and relaxed to the ground-state configuration using the conjugate-gradient algorithm. The three bottom layers of CZTS$_{0.25}$Se$_{0.75}$ slabs were permanently fixed in bulklike positions and passivated by H atoms to simulate continuous bulk. The amorphous MoO_3 (a-MoO_3) sample was generated by DFT molecular-dynamics (DFT-MD) simulations using the melt-and-quench approach. The system with randomly placed Mo and O atoms at artificially low density, $3.70/(1.5)^3$ g/cm^3, was annealed at 1300 K for 1000 fs, providing good intermixing. After being rescaled to the normal density of 3.70 g/cm^3, the system was annealed at 1300 K for 3000 fs, cooled to 0 K for 15000 fs, and relaxed to the ground-state configuration below the 0.05 eV/A force tolerance level. The amorphous density was validated by preparing several sacrificial a-MoO_3 samples and relaxing them at variable volume, confirming the stability of the 3.70 g/cm^3 density. The electronic structure for the generated sample was calculated using both PBE and HSE06 functionals, confirming a defect-free band gap.

■ RESULTS AND DISCUSSION

Back interfaces for as-grown films with Mo/glass substrates were characterized first via cross-sectional nano-Auger and KPFM measurements. Figure 2a displays the secondary electron micrograph as well as elemental maps for Cu, Zn, S, Se, and Mo measured on a sloped cross-section prepared by cryo-FIB (8° angle of incidence for the ion beam) on as-grown CZTSSe thin films. The elemental maps as well as Auger line scans confirm the presence of a region between Mo and CZTSSe where only Mo, Se, and S are present. This is consistent with the formation of a Mo(S,Se)$_2$ interlayer between Mo and CZTSSe by the direct reaction between the chalcogens (S and Se) from the precursor ink and the Mo substrate during the film growth.[47,48] Due to the nature of its formation, close control over the thickness and quality of this Mo(S,Se)$_2$ interlayer is challenging, thereby inhibiting reproducibility in the device performance levels.[49] Figure 2b shows the topography and surface potential maps for a sloped CZTSSe/Mo(S,Se)$_2$/Mo cross-section of an as-grown film with a 5° angle of incidence. In the surface potential maps, three regions can be identified: Mo, Mo(S,Se)$_2$, and CZTSSe. The Mo(S,Se)$_2$ interlayer surface potential is about 520 meV smaller than that of Mo (520 meV larger work function) and 260 meV smaller than that of CZTSSe (260 meV larger work function). Therefore, the Mo(S,Se)$_2$ interlayer is expected to induce an upward band bending of about 260 meV in the CZTSSe adjacent to the back interface. On the basis of the KPFM measurements in conjunction with previous reports on the band edge position measurements for CZTSSe and Mo(S,Se)$_2$ via photoemission spectroscopy,[33,50−52] a band structure for the CZTSSe/Mo(S,Se)$_2$/Mo interfaces is proposed in Figure 2c (details of the band structure derivation are given in the Supporting Information). As shown in the band diagram in Figure 2c, there is a large downward band bending at the Mo(S,Se)$_2$/Mo interface that inhibits the hole transport to the Mo metal electrode except for very thin Mo(S,Se)$_2$ layers where hole tunneling could occur from the CZTSSe to the Mo (dashed arrow in the diagram), forming a quasi-Ohmic contact.[34,53] Therefore, although the Mo(S,Se)$_2$ back contact layer can induce a fairly large upward band bending near the back surface, its thickness needs to be well-controlled (few hundred nanometers) to not block the hole transfer to the Mo electrode.[47] As mentioned above, since Mo(S,Se)$_2$ is not directly deposited on the CZTSSe, proper thickness control could be challenging.

To determine the composition of the CZTSSe adjacent to the back interface, solution-deposited films were mechanically exfoliated along the CZTSSe/Mo(S,Se)$_2$ interfaces. A schematic of the CZTSSe device exfoliation procedure is shown in the Supporting Information (Figure S1). The local Auger spectroscopy results confirm that exfoliation occurs between CZTSSe and Mo(S,Se)$_2$, since the layer remaining on top of the glass substrate is composed of Mo(S,Se)$_2$ (Supporting Information, Figure S4) and no Mo was found on the exfoliated CZTSSe surfaces. This is consistent with the poor adhesion between Mo(S,Se)$_2$ and CZTSSe. Figure 3a displays the SEM micrograph and nano-Auger elemental maps for the CZTSSe back surface immediately after exfoliation (denoted as "As-exfoliated"). The back surface exhibited a mesa−valley structure where the mesas are Se-rich while the valleys are enriched in
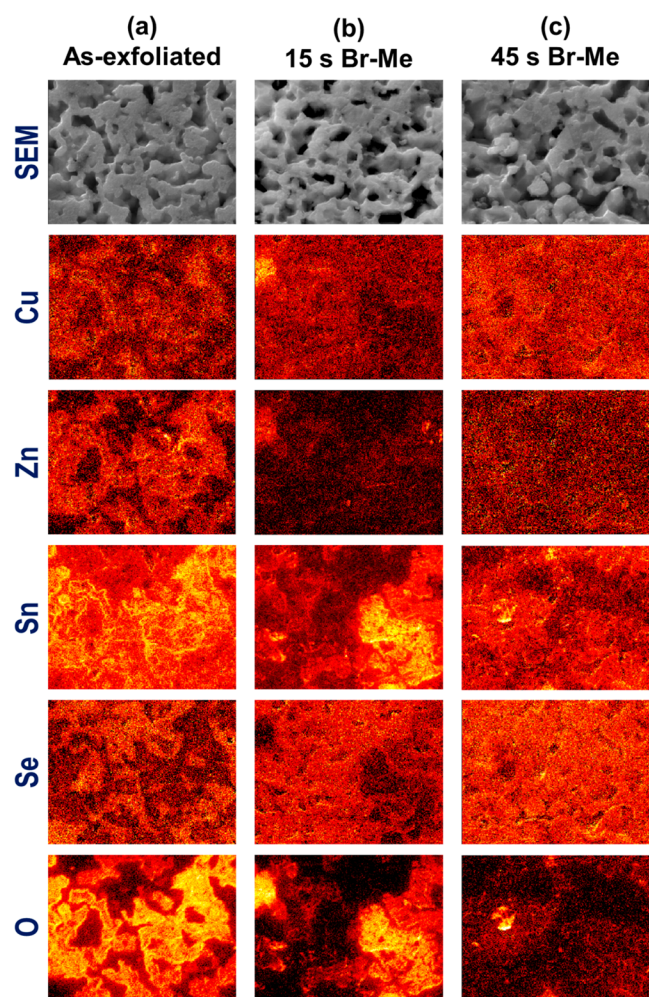
Figure 3. Nano-Auger elemental maps on exfoliated CZTSSe surfaces: secondary electron micrograph and Auger elemental maps for Cu, Zn, Sn, Se, and O for surfaces after (a) exfoliation, (b) 15 s of Br–Me etching, and (c) 45 s of Br–Me etching.

Cu, Zn, and O. The presence of valleys in the planar SEM micrograph is consistent with the observation of the voids in the cross-sectional measurements shown in Figure 2. Variations in Sn distribution across the mesas and valleys are less dramatic, with only slight signal intensity enhancements in the valleys. Considering the smaller escape depth for Sn and O Auger electrons (∼1 nm) compared to the other elements mapped here (≥2 nm), it can be concluded that the back surface, particularly in the valleys, is terminated with a thin layer of SnO_x (or $SnSe_{2-x}O_x$). The back surface morphology and composition are controlled by liquid-phase reactions during the thin-film growth process as well as the solid-state reactions near the back surface throughout the postdeposition annealing steps. Subtler compositional and morphological variations were observed on exfoliated thermally evaporated CZTSe films (Figure S5, Supporting Information), consistent with the strong influence of the growth method on the properties of the back surfaces. However, regardless of the growth method, Sn and O enrichment at the back surface has been observed, which could be due to solid-state reactions during the annealing processes where O is supplied by the ambient (in the air annealing process) or soda lime glass substrate, in agreement with the observation of larger O concentrations near the back interface in cross-sectional nano-Auger measurements even prior to exfoliation (see Figure S6, Supporting Information).[18]

Large levels of compositional nonuniformity at the back interface could result in high recombination velocities which limit the hole transport to the buffer layer.[54] The back surface composition can be modified by immersing the exfoliated films in 0.125 M Br–Me for 15 and 45 s, as shown in Figure 3b,c. After 45 s of Br–Me etching, the back surface composition became more uniform and the majority of the back surface oxide was removed. The Br–Me etching mechanism for selenide compounds is described as a two-step process that includes preferential etching of metals (i.e., Cu, Zn, and Sn) in the form of soluble bromides followed by halogenation of the Se^0 or SeO_2.[21,55,56] For surfaces terminated with a thin layer of SnO_x (or $SnSe_{2-x}O_x$), Br–Me etching could attack the metal-rich layer underneath the oxide, therefore removing the oxide
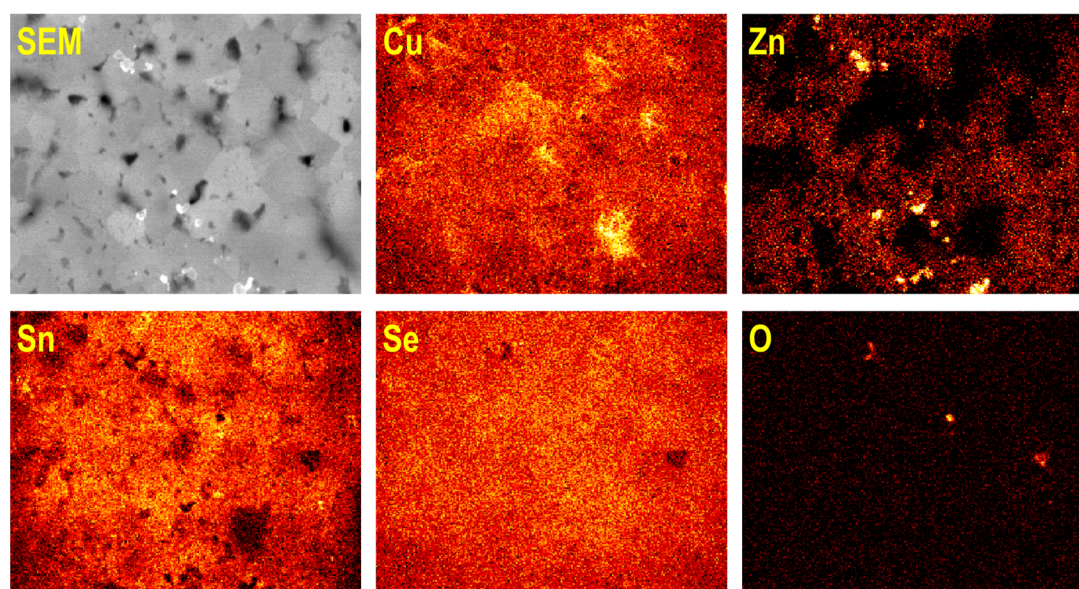

Figure 4. Nano-Auger elemental maps of CMP-treated CZTSSe surfaces: secondary electron micrograph and Auger elemental maps for Cu, Zn, Sn, Se, and O for an exfoliated CZTSSe surface after 10 min of CMP treatment.
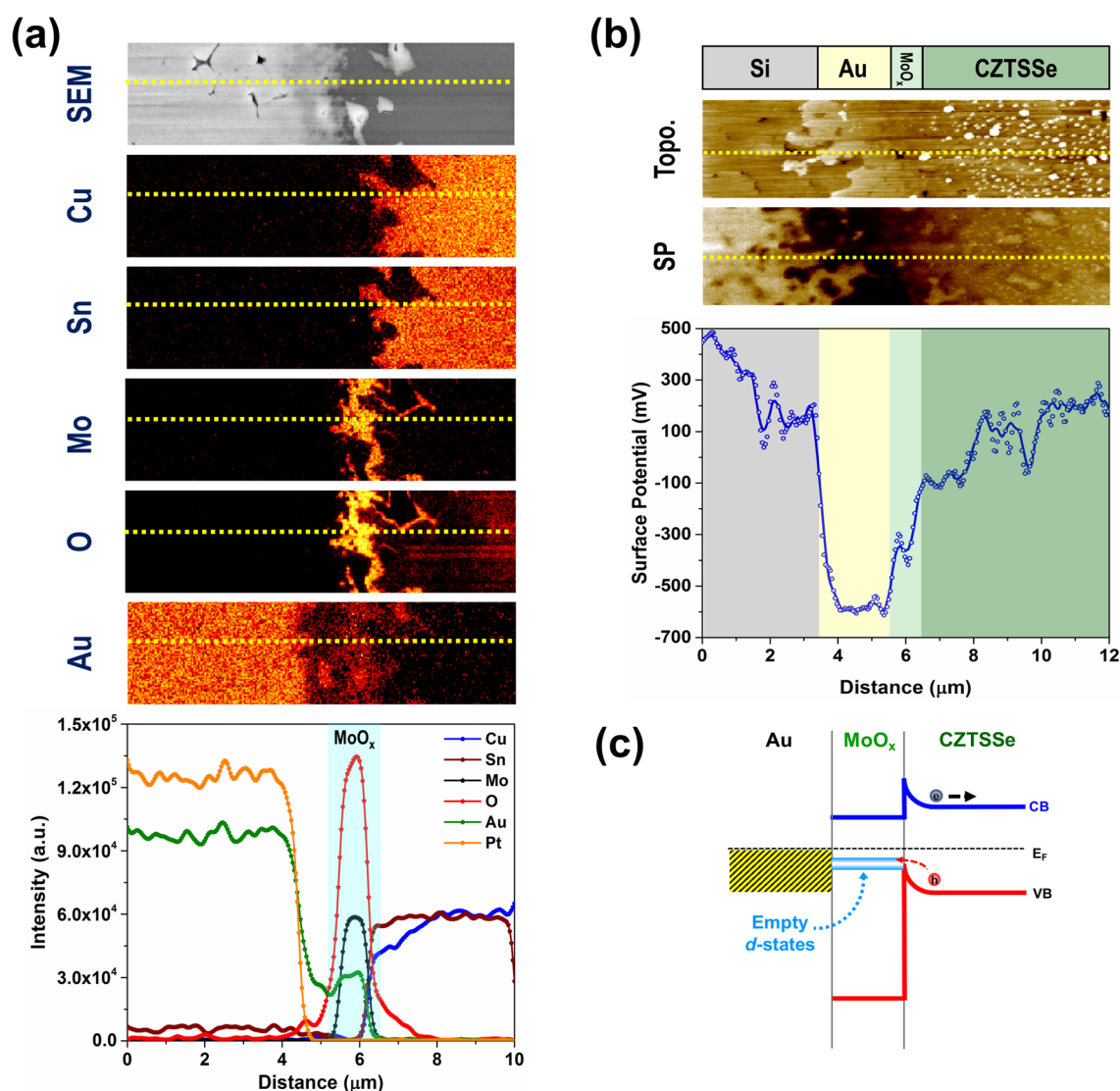
Figure 5. Cross-sectional nano-Auger and KPFM measurements for the Au/Mo/CZTSSe interface: (a) SEM micrograph and elemental maps measured by nano-Auger on the cross-section (a line scan (dotted line) measured for Cu, Sn, Mo, O and Au is shown at the bottom); (b) topography and surface potential (SP) maps measured by KPFM on the cross-sections (a line scan (dotted line) extracted from the SP measurements is shown at the bottom); (c) estimated band diagram for the interface derived from the measured work function values beside the band edge positions measured by femtosecond ultraviolet spectroscopy in ref 17. Cross-sections were prepared by grazing angle of incidence cryo-FIB with a 4° angle of incidence.

layer by a lift-off mechanism. The improvement in compositional uniformity is confirmed by the pixel analysis of the Cu, Zn, Sn, and Se elemental maps for all three measurement steps (Figure S7, Supporting Information) where the pixel density distribution range became narrower with 45 s of Br−Me etching. It should be noted that Br−Me etching occurs preferentially in the valleys, since a larger density of deep valleys is evident even after 15 s of etching. Due to this vertical etching effect, the Br−Me etching time should be limited to less than 1 min.

While a higher density of valleys (and higher interface roughness) can enhance the internal reflection, it could prevent formation of a conformal high-work-function contact layer on the kesterite absorbers, thereby having a negative impact on the junction's electronic quality.[57] As an alternative, chemical-mechanical polishing (CMP) of exfoliated surfaces was investigated to prepare flat exfoliated surfaces prior to contact deposition. Figure 4 displays the nano-Auger secondary

electron micrograph and elemental maps for Cu, Zn, Sn, Se, and O for an exfoliated CZTSSe surface treated with 10 min of CMP using a polish slurry composed of dilute HCl and Al_2O_3 abrasive particles. Despite formation of a relatively smooth and O-free surface, nonuniformities in Cu, Zn, and Sn distributions are observed after CMP treatment. In particular, a considerable fraction of the surface appears to be Cu-rich and/or Sn-rich, which could be attributed to local formation of $CuSe_y$ and Cu_xSnSe_y secondary phases after CMP (local spectroscopy results are shown in the Supporting Information, Figure S8). This is consistent with selective etching of Zn-rich phases by the HCl solution.[21,58] Therefore, although CMP treatment could effectively prepare very flat absorber/contact interfaces, it is unable to achieve compositional uniformity.

To realize larger upward band bending for enhanced hole extraction, 40 nm thick MoO_3 and 200 nm Au blanket films were deposited onto the exfoliated CZTSSe surfaces by thermal evaporation. To minimize any thermally activated elemental
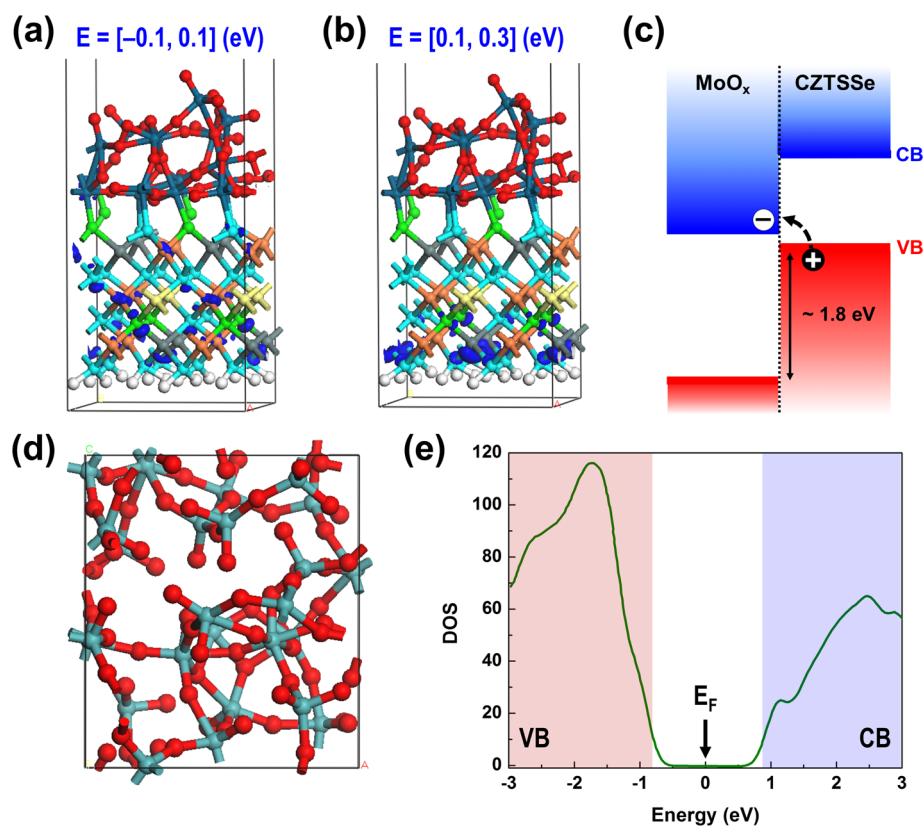
Figure 6. DFT simulation of MoO_x/CZTSSe interfaces and amorphous MoO_3: MoO_x/CZTSSe stacks with band-decomposed charge density visualized as blue spots for states within the energy ranges (a) −0.1 to +0.1 eV and (b) 0.1 to 0.3 eV; (c) band alignment between MoO_x and CZTSSe estimated from local DOS calculations; (d) atomic structure for a-MoO_3 with a bulk density of 3.70 g/cm³ where Mo and O atoms are shown as green and red spheres, respectively; (e) bulk DOS calculated by PBE for a-MoO_3 with a 3.70 g/cm³ density. The valence band maximum (VBM) and conduction band minimum (CBM) are at −0.91 and +0.96 eV, respectively, leading to an estimated band gap of 1.87 eV.

intermixing at the interfaces, besides natural heating due to the thermal evaporation processes (temperature <70 °C), samples were not subjected to any thermal treatment during or after the Au/MoO_3 evaporation. Since Br−Me etching is more effective in achieving uniform elemental distributions, exfoliated films were treated with 45 s of Br−Me etching prior to MoO_3 deposition. Figure 5a shows the cross-sectional nano-Auger secondary electron and elemental maps for Cu, Sn, Mo, O, and Au on the Au/MoO_3/CZTSSe sloped cross-section; a line scan taken along the yellow dotted line is also shown. The line scan includes Pt as well as Au since a thin sacrificial layer of Pt/Ti was sputtered on top of the Au blankets prior to cryo-FIB milling. It should be noted that there is an overlap between the primary Au Auger peaks used for the line scan measurements and a secondary Pt peak, resulting in a strong Au signal within the Pt layer. Both the maps and the line scan indicate the presence of a MoO_x layer that has an abrupt and conformal interface with CZTSSe. In contrast, the transition from the Au to the MoO_x is gradual, with a large concentration of Au present within the MoO_x region.

The topography and surface potential maps as well as a surface potential line scan (along the dotted line) measured by cross-sectional KPFM on Au/MoO_3/CZTSSe interfaces are displayed in Figure 5b. For this sample, instead of Pt/Ti, a Pt/Si/Ti blanket was sputtered prior to cryo-FIB cross-sectioning. A closer look at the line scan reveals that the MoO_x layer's work function is about 230 meV smaller than the Au work function. This is in contrast to the previous reports that estimated the MoO_3 work function to be at least 1 eV larger than that of

Au.[59,60] Besides the substoichiometric nature of this oxide (O/ Mo < 3) and air exposure between the evaporation steps, such low work function levels for the MoO_x could be in part due to the significant amount of Au incorporation.[61] According to the measured work functions and band edge positions (measured by femtosecond ultraviolet photoelectron spectroscopy (fs-UPS)[17,62]), an approximate band diagram has been proposed in Figure 5c. Despite Au incorporation, the Au/MoO_x contact layer is estimated to induce 400 meV upward band bending in the CZTSSe adjacent to the contact/absorber interface. Since the MoO_x used in this study is oxygen-deficient, the hole conduction can occur via the empty Mo d-states present due to a large concentration of oxygen vacancies.[63,64] XPS and fs-UPS measurements have shown that the d-state band is about 200 meV below the Fermi level.[17] The CZTSSe valence band appears to be well-positioned relative to the conductive defect state band in MoO_x, therefore enabling effective hole extraction from the back surface. However, it should be noted that the enhanced upward band bending and proper band alignment can be compromised by the detrimental effect of Au−MoO_x intermixing, leading to formation of a barrier between Au and CZTSSe for a significant fraction of the interface. This necessitates exploration of alternative contact electrodes in combination with MoO_x.

To observe the impact of enhanced upward band bending near the hole transport layer in the PV performance of CZTSSe solar cells, J−V characteristics were evaluated before and after exfoliation for a 2 μm thick film (Supporting Information, Figure S9). Before exfoliation, the CZTSSe cell showed V_{oc} =

452 mV, J_{sc} = 34 mA/cm^2, FF = 61%, and PCE = 9.3%. In comparison, exfoliation, followed by Br−Me etching and MoO$_3$/Au deposition, resulted in V_{oc} = 454 mV, J_{sc} = 38 mA/cm^2, FF = 55%, and PCE = 9.7%. While the change in V_{oc} is negligible (consistent with the simulations shown in Figure 1), the FF was reduced by 6%, possibly because of Au−MoO$_x$ intermixing that increased the conductivity of the hole transport layer and therefore enhanced the shunt conductance. However, the power conversion efficiency saw a 0.4% boost mainly due to the 4 mA/cm^2 increase in J_{sc}. This increase in J_{sc} can be attributed to the fact that the Au back electrode in the exfoliated devices is a very good infrared reflector which returns the transmitting infrared photons from the back surface to be absorbed by CZTSSe.[17] Although these results confirm the possibility of realizing working devices via mechanical exfoliation, there are several practical challenges that need to be addressed to observe significant improvements in PV performance: (i) crack formation within the CZTSSe film during the exfoliation process; (ii) lack of reliable thinning methods for reducing the thickness of 2 μm after exfoliation without pinhole or crack formation; (iii) pinhole formation in the case of growing films thinner than 2 μm prior to exfoliation. These challenges have been discussed in more detail in refs 17 and 62.

The MoO$_x$/CZTSSe interfaces were evaluated by DFT simulations where a bilayer comprised of eight MoO$_2$ and, subsequently, eight MoO$_3$ molecules was brought into contact with S/Se-terminated CZTSSe surfaces. The MoO$_2$ was in direct contact with a S/Se-terminated CZTSSe so that the Mo atoms could form bonds to S/Se while maintaining their bulklike charge state. As shown in Figure 6a, the interface between MoO$_x$ and CZTSSe is near-ideal with direct Mo−S and Mo−Se interfacial bonds. In addition, no dangling bond is found at the interface. The band-decomposed charge density for two energy ranges of −0.1 to +0.1 eV and 0.1 eV−0.3 eV showed that no state is present at the interface (blue regions in Figure 6a,b). By evaluating the variations in the local density of state (DOS) curves calculated for four different layers in the MoO$_x$/CZTSSes structure, the valence band offset between the CZTSSe and MoO$_x$ is estimated as 1.87 eV (Supporting Information Figure S10 displays the four layers and corresponding DOS curves). On the basis of the calculated valence band offset and band gaps,[9] the band alignment shown in Figure 6c is estimated. The small offset between the CZTSSe valence band (VB) and MoO$_x$ conduction band (CB) is consistent with the observation of no band gap in DOS calculations for the MoO$_x$/CZTSSe structure (Supporting Information, Figure S11). Considering that the Fermi level in CZTSSe is about 0.5 eV above the edge of the VB, a minimum 100 meV upward band bending is expected even for such an atomically thin MoO$_x$ overlayer.[51]

To further explain the propensity of Au diffusion into the MoO$_x$ contact layer, DFT calculations were used to model the structure of bulk amorphous MoO$_3$ (a-MoO$_3$). Parts d and e of Figure 6 display the atomic structures for a-MoO$_3$ with a bulk density of 3.70 g/cm^3. Amorphous MoO$_3$ was particularly chosen considering that the films used in this study were deposited at temperatures no higher than 70 °C by thermal evaporation. In this structure, a large void space can be observed whose dimensions are larger than the radius of Au atoms, consistent with the high permeability of the MoO$_3$ to Au in-diffusion. Furthermore, owing to the 2D-like layered structured with large interlayer spacing, even a crystalline

MoO$_3$ layer might not act as a barrier to Au diffusion.[60] Therefore, other metal electrodes with larger ionic radii than that of Au and work functions close to that of Au need to be explored for use with MoO$_3$.

CONCLUSION

In summary, a unique combination of nanocharacterization tools, including nano-Auger, KPFM, and cryo-FIB measurements, were employed to determine the electronics and chemistry of the back interfaces in thin-film kesterite solar cells and gauge the possibility of surface potential modification in the absorber via direct deposition of high-work-function metal oxides on exfoliated surfaces. Cross-sectional nano-Auger and KPFM measurements indicated that a thick Mo(S,Se)$_2$ layer forms between the CZTSSe and Mo, which induces about 240 meV upward band bending in the CZTSSe layer, while forming a 450 meV barrier for the hole transfer into the Mo electrode. To deposit a high-work-function alternative contact layer, mechanical exfoliation was employed, wherein cleavage occurred at the interface between Mo(S,Se)$_2$ and CZTSSe. Planar nano-Auger measurements showed considerable levels of compositional nonuniformities on the exfoliated surfaces. This compositional nonuniformity was minimized by short Br−Me etching of the surfaces. Cross-sectional nano-Auger and KPFM measurements on Au/MoO$_3$/CZTSSe blankets showed an upward band bending of about 400 meV within the CZTSSe layer, despite substantial Au incorporation into the MoO$_x$ layer. DFT simulations of the atomic structure for bulk amorphous MoO$_3$ showed the presence of large voids within the structure that enable Au in-diffusion. With employment of less diffusive metal electrodes such as Pt or Pd, upward band bending beyond 500 meV is expected to be achieved.

ASSOCIATED CONTENT

ⓢ Supporting Information

The Supporting Information is available free of charge on the ACS Publications website at DOI: 10.1021/acsami.7b01838.

> Schematics that explain the exfoliation and cryo-FIB cross-sectioning processes, local Auger spectra of exfoliated surfaces and cross-sections of CZTSSe, pixel brightness analysis for Cu, Zn, Sn, and Se elemental maps measured before and after Br−Me treatment, planar and cross-sectional nano-Auger elemental maps for CZTSSe films grown by thermal evaporation, J−V charateristics of exofiliated CZTSSe devices, and atomic structure and local DOS for MoO$_x$/CZTSSe simulated by DFT (PDF)

AUTHOR INFORMATION

Corresponding Author

*E-mail: akummel@ucsd.edu.

ORCID

Andrew C. Kummel: 0000-0001-8301-9855

Notes

The authors declare no competing financial interest.

■ REFERENCES

(1) Ramanujam, J.; Verma, A.; Gonzalez-Diaz, B.; Guerrero-Lemus, R.; del Canizo, C.; Garcia-Tabares, E.; Rey-Stolle, I.; Granek, F.; Korte, L.; Tucci, M.; Rath, J.; Singh, U. P.; Todorov, T.; Gunawan, O.; Rubio, S.; Plaza, J. L.; Dieguez, E.; Hoffmann, B.; Christiansen, S.; Cirlin, G. E. Inorganic Photovoltaics - Planar and Nanostructured Devices. *Prog. Mater. Sci.* **2016**, *82*, 294−404.

(2) Shah, A.; Torres, P.; Tscharner, R.; Wyrsch, N.; Keppner, H. Photovoltaic Technology: The Case for Thin-Film Solar Cells. *Science* **1999**, *285* (5428), 692−698.

(3) Fthenakis, V. Sustainability of Photovoltaics: The Case for Thin-Film Solar Cells. *Renewable Sustainable Energy Rev.* **2009**, *13* (9), 2746−2750.

(4) Mitzi, D. B.; Gunawan, O.; Todorov, T. K.; Barkhouse, D. A. R. Prospects and Performance Limitations for Cu-Zn-Sn-S-Se Photovoltaic Technology. *Philos. Trans. R. Soc., A* **2013**, *371* (1996), 20110432.

(5) Jackson, P.; Wuerz, R.; Hariskos, D.; Lotter, E.; Witte, W.; Powalla, M. Effects of Heavy Alkali Elements in Cu(In,Ga)Se2 Solar Cells with Efficiencies up to 22.6%. *Phys. Status Solidi RRL* **2016**, *10* (8), 583−586.

(6) Green, M. A.; Emery, K.; Hishikawa, Y.; Warta, W.; Dunlop, E. D. Solar Cell Efficiency Tables (Version 48). *Prog. Photovoltaics* **2016**, *24* (7), 905−913.

(7) Liu, X. L.; Feng, Y.; Cui, H. T.; Liu, F. Y.; Hao, X. J.; Conibeer, G.; Mitzi, D. B.; Green, M. The Current Status and Future Prospects of Kesterite Solar Cells: A Brief Review. *Prog. Photovoltaics* **2016**, *24* (6), 879−898.

(8) Wang, W.; Winkler, M. T.; Gunawan, O.; Gokmen, T.; Todorov, T. K.; Zhu, Y.; Mitzi, D. B. Device Characteristics of CZTSSe Thin-Film Solar Cells with 12.6% Efficiency. *Adv. Energy Mater.* **2014**, *4* (7), 1301465.

(9) Chagarov, E.; Sardashti, K.; Kummel, A. C.; Lee, Y. S.; Haight, R.; Gershon, T. S. Ag2ZnSn(S,Se)4: A Highly Promising Absorber for Thin Film Photovoltaics. *J. Chem. Phys.* **2016**, *144* (10), 104704.

(10) Gokmen, T.; Gunawan, O.; Todorov, T. K.; Mitzi, D. B. Band Tailing and Efficiency Limitation in Kesterite Solar Cells. *Appl. Phys. Lett.* **2013**, *103* (10), 103506.

(11) Schorr, S. The Crystal Structure of Kesterite Type Compounds: A Neutron and X-Ray Diffraction Study. *Sol. Energy Mater. Sol. Cells* **2011**, *95* (6), 1482−1488.

(12) Guchhait, A.; Su, Z.; Tay, Y. F.; Shukla, S.; Li, W. J.; Leow, S. W.; Tan, J. M. R.; Lie, S.; Gunawan, O.; Wong, L. H. Enhancement of Open-Circuit Voltage of Solution-Processed Cu2ZnSnS4 Solar Cells with 7.2% Efficiency by Incorporation of Silver. *ACS Energy Lett.* **2016**, *1* (6), 1256−1261.

(13) Chen, S. Y.; Walsh, A.; Gong, X. G.; Wei, S. H. Classification of Lattice Defects in the Kesterite Cu2ZnSnS4 and Cu2znsnse4 Earth-Abundant Solar Cell Absorbers. *Adv. Mater.* **2013**, *25* (11), 1522−1539.

(14) Chen, S. Y.; Yang, J. H.; Gong, X. G.; Walsh, A.; Wei, S. H. Intrinsic Point Defects and Complexes in the Quaternary Kesterite Semiconductor Cu2ZnSnS4. *Phys. Rev. B: Condens. Matter Mater. Phys.* **2010**, *81* (24), 245204.

(15) Shin, D.; Saparov, B.; Mitzi, D. B. Defect Engineering in Multinary Earth-Abundant Chalcogenide Photovoltaic Materials. *Adv. Energy Mater.* **2017**, 1602366.

(16) Yuan, Z. K.; Chen, S. Y.; Xiang, H. J.; Gong, X. G.; Walsh, A.; Park, J. S.; Repins, I.; Wei, S. H. Engineering Solar Cell Absorbers by Exploring the Band Alignment and Defect Disparity: The Case of Cu- and Ag-Based Kesterite Compounds. *Adv. Funct. Mater.* **2015**, *25* (43), 6733−6743.

(17) Antunez, P. D.; Lee, Y. S.; Bishop, D. M.; Gokmen, T.; Gunawan, O.; Gershon, T. S.; Todorov, T. K.; Singh, S.; Haight, R. Back Contact Engineering for Increased Performance in CZTSSe Solar Cells. *Adv. Energy Mater.* **2017**, 1602585.

(18) Sardashti, K.; Haight, R.; Gokmen, T.; Wang, W.; Chang, L. Y.; Mitzi, D. B.; Kummel, A. C. Impact of Nanoscale Elemental Distribution in High-Performance Kesterite Solar Cells. *Adv. Energy Mater.* **2015**, *5* (10), 1402180.

(19) Simchi, H.; McCandless, B. E.; Meng, T.; Shafarman, W. N. Structure and Interface Chemistry of Moo3 Back Contacts in Cu(In,Ga)Se2 Thin Film Solar Cells. *J. Appl. Phys.* **2014**, *115* (3), 033514.

(20) Yang, R. L.; Wang, D. Z.; Jeng, M. J.; Ho, K. M.; Wang, D. L. Stable Cdte Thin Film Solar Cells with a MoOx Back-Contact Buffer Layer. *Prog. Photovoltaics* **2016**, *24* (1), 59−65.

(21) Mousel, M.; Redinger, A.; Djemour, R.; Arasimowicz, M.; Valle, N.; Dale, P.; Siebentritt, S. Hcl and Br-2-Meoh Etching of Cu2ZnSnSe4 Polycrystalline Absorbers. *Thin Solid Films* **2013**, *535*, 83−87.

(22) Mousel, M.; Schwarz, T.; Djemour, R.; Weiss, T. P.; Sendler, J.; Malaquias, J. C.; Redinger, A.; Cojocaru-Miredin, O.; Choi, P. P.; Siebentritt, S. Cu-Rich Precursors Improve Kesterite Solar Cells. *Adv. Energy Mater.* **2014**, *4* (2), 1300543.

(23) Kroger, M.; Hamwi, S.; Meyer, J.; Riedl, T.; Kowalsky, W.; Kahn, A. Role of the Deep-Lying Electronic States of Moo3 in the Enhancement of Hole-Injection in Organic Thin Films. *Appl. Phys. Lett.* **2009**, *95* (12), 123301.

(24) Simchi, H.; McCandless, B. E.; Meng, T.; Shafarman, W. N. Structural, Optical, and Surface Properties of WO3 Thin Films for Solar Cells. *J. Alloys Compd.* **2014**, *617*, 609−615.

(25) Simchi, H.; McCandless, B. E.; Meng, T.; Boyle, J. H.; Shafarman, W. N. Characterization of Reactively Sputtered Molybdenum Oxide Films for Solar Cell Application. *J. Appl. Phys.* **2013**, *114* (1), 013503.

(26) Hurtig, N. C.; Williams-Jones, A. E. An Experimental Study of the Solubility of MoO3 in Aqueous Vapour and Low to Intermediate Density Supercritical Fluids. *Geochim. Cosmochim. Acta* **2014**, *136*, 169−193.

(27) Erfurth, F.; Jehl, Z.; Bouttemy, M.; Dahan, N.; Tran-Van, P.; Gerard, I.; Etcheberry, A.; Greffet, J. J.; Powalla, M.; Voorwinden, G.; Lincot, D.; Guillemoles, J. F.; Naghavi, N. Mo/Cu(In,Ga)Se2 Back Interface Chemical and Optical Properties for Ultrathin Cigse Solar Cells. *Appl. Surf. Sci.* **2012**, *258* (7), 3058−3061.

(28) Osada, S.; Abe, Y.; Anegawa, T.; Minemoto, T.; Takakura, H. Cu(In,Ga)Se-2 Solar Cells with Superstrate Structure Using Lift-Off Process. *Sol. Energy Mater. Sol. Cells* **2011**, *95* (1), 223−226.

(29) Fuertes Marron, D.; Meeder, A.; Sadewasser, S.; Wurz, R.; Kaufmann, C. A.; Glatzel, T.; Schedel-Niedrig, T.; Lux-Steiner, M. C. Lift-Off Process and Rear-Side Characterization of CuGaSe2 Chalcopyrite Thin Films and Solar Cells. *J. Appl. Phys.* **2005**, *97* (9), 094915.

(30) Caballero, R.; Nichterwitz, M.; Steigert, A.; Eicke, A.; Lauermann, I.; Schock, H. W.; Kaufmann, C. A. Impact of Na on MoSe2 Formation at the CIGSe/Mo Interface in Thin-Film Solar Cells on Polyimide Foil at Low Process Temperatures. *Acta Mater.* **2014**, *63*, 54−62.

(31) Miller, D. W.; Warren, C. W.; Gunawan, O.; Gokmen, T.; Mitzi, D. B.; Cohen, J. D. Electronically Active Defects in the Cu2ZnSn-(Se,S)4 Alloys as Revealed by Transient Photocapacitance Spectroscopy. *Appl. Phys. Lett.* **2012**, *101* (14), 142106.

(32) Winkler, M. T.; Wang, W.; Gunawan, O.; Hovel, H. J.; Todorov, T. K.; Mitzi, D. B. Optical Designs That Improve the Efficiency of Cu2ZnSn(S,Se)4 Solar Cells. *Energy Environ. Sci.* **2014**, 7 (3), 1029–1036.

(33) Gershon, T.; Sardashti, K.; Gunawan, O.; Mankad, R.; Singh, S.; Lee, Y. S.; Ott, J. A.; Kummel, A.; Haight, R. Photovoltaic Device with over 5% Efficiency Based on an n-Type Ag2ZnSnSe4 Absorber. *Adv. Energy Mater.* **2016**, 6, 1601182.

(34) Sardashti, K.; Haight, R.; Anderson, R.; Contreras, M.; Fruhberger, B.; Kummel, A. C. Grazing Incidence Cross-Sectioning of Thin-Film Solar Cells via Cryogenic Focused Ion Beam: A Case Study on CIGSe. *ACS Appl. Mater. Interfaces* **2016**, 8 (24), 14994–14999.

(35) Todorov, T. K.; Reuter, K. B.; Mitzi, D. B. High-Efficiency Solar Cell with Earth-Abundant Liquid-Processed Absorber. *Adv. Mater.* **2010**, 22 (20), E156–E159.

(36) Todorov, T. K.; Tang, J.; Bag, S.; Gunawan, O.; Gokmen, T.; Zhu, Y.; Mitzi, D. B. Beyond 11% Efficiency: Characteristics of State-of-the-Art Cu2ZnSn(S,Se)4 Solar Cells. *Adv. Energy Mater.* **2013**, 3 (1), 34–38.

(37) Minj, A.; Cros, A.; Auzelle, T.; Pernot, J.; Daudin, B. Direct Assessment of p−n Junctions in Single GaN Nanowires by Kelvin Probe Force Microscopy. *Nanotechnology* **2016**, 27 (38), 385202.

(38) Melitz, W.; Shen, J.; Kummel, A. C.; Lee, S. Kelvin Probe Force Microscopy and Its Application. *Surf. Sci. Rep.* **2011**, 66 (1), 1–27.

(39) Sardashti, K.; Paul, D.; Hitzman, C.; Hammond, J.; Haight, R.; Kummel, A. C. Nano-Scale Compositional Analysis of Surfaces and Interfaces in Earth-Abundant Kesterite Solar Cells. *J. Mater. Res.* **2016**, 31 (22), 3473–3481.

(40) Perdew, J. P.; Burke, K.; Ernzerhof, M. Generalized Gradient Approximation Made Simple (Vol 77, Pg 3865, 1996). *Phys. Rev. Lett.* **1997**, 78 (7), 1396–1396.

(41) Perdew, J. P.; Burke, K.; Ernzerhof, M. Generalized Gradient Approximation Made Simple. *Phys. Rev. Lett.* **1996**, 77 (18), 3865–3868.

(42) Blochl, P. E. Projector Augmented-Wave Method. *Phys. Rev. B: Condens. Matter Mater. Phys.* **1994**, 50 (24), 17953–17979.

(43) Kresse, G.; Joubert, D. From Ultrasoft Pseudopotentials to the Projector Augmented-Wave Method. *Phys. Rev. B: Condens. Matter Mater. Phys.* **1999**, 59 (3), 1758–1775.

(44) Kresse, G.; Furthmuller, J. Efficiency of Ab-Initio Total Energy Calculations for Metals and Semiconductors Using a Plane-Wave Basis Set. *Comput. Mater. Sci.* **1996**, 6 (1), 15–50.

(45) Kresse, G.; Furthmuller, J. Efficient Iterative Schemes for Ab Initio Total-Energy Calculations Using a Plane-Wave Basis Set. *Phys. Rev. B: Condens. Matter Mater. Phys.* **1996**, 54 (16), 11169–11186.

(46) Krukau, A. V.; Vydrov, O. A.; Izmaylov, A. F.; Scuseria, G. E. Influence of the Exchange Screening Parameter on the Performance of Screened Hybrid Functionals. *J. Chem. Phys.* **2006**, 125 (22), 224106.

(47) Shin, B.; Bojarczuk, N. A.; Guha, S. On the Kinetics of MoSe2 Interfacial Layer Formation in Chalcogen-Based Thin Film Solar Cells with a Molybdenum Back Contact. *Appl. Phys. Lett.* **2013**, 102 (9), 091907.

(48) Shin, B.; Zhu, Y.; Bojarczuk, N. A.; Chey, S. J.; Guha, S. Control of an Interfacial MoSe2 Layer in Cu2ZnSnSe4 Thin Film Solar Cells: 8.9% Power Conversion Efficiency with a Tin Diffusion Barrier. *Appl. Phys. Lett.* **2012**, 101 (5), 053903.

(49) Yoon, J. H.; Park, J. K.; Kim, W. M.; Lee, J.; Pak, H.; Jeong, J. H. Characterization of Efficiency-Limiting Resistance Losses in Mono-lithically Integrated Cu(In,Ga)Se2 Solar Modules. *Sci. Rep.* **2015**, 5, 07690.

(50) Haight, R.; Barkhouse, A.; Gunawan, O.; Shin, B.; Copel, M.; Hopstaken, M.; Mitzi, D. B. Band Alignment at the Cu2ZnSn(SxSe1-X)(4)/CdS Interface. *Appl. Phys. Lett.* **2011**, 98 (25), 253502.

(51) Haight, R.; Shao, X. Y.; Wang, W.; Mitzi, D. B. Electronic and Elemental Properties of the Cu2ZnSn(S,Se)4 Surface and Grain Boundaries. *Appl. Phys. Lett.* **2014**, 104 (3), 033902.

(52) Chirila, A.; Buecheler, S.; Pianezzi, F.; Bloesch, P.; Gretener, C.; Uhl, A. R.; Fella, C.; Kranz, L.; Perrenoud, J.; Seyrling, S.; Verma, R.; Nishiwaki, S.; Romanyuk, Y. E.; Bilger, G.; Tiwari, A. N. Highly Efficient Cu(In,Ga)Se2 Solar Cells Grown on Flexible Polymer Films. *Nat. Mater.* **2011**, 10 (11), 857–861.

(53) Hsiao, K. J.; Liu, J. D.; Hsieh, H. H.; Jiang, T. S. Electrical Impact of MoSe2 on Cigs Thin-Film Solar Cells. *Phys. Chem. Chem. Phys.* **2013**, 15 (41), 18174–18178.

(54) Kanevce, A.; Repins, I.; Wei, S. H. Impact of Bulk Properties and Local Secondary Phases on the Cu2(Zn,Sn)Se4 Solar Cells Open-Circuit Voltage. *Sol. Energy Mater. Sol. Cells* **2015**, 133, 119–125.

(55) Bouttemy, M.; Tran-Van, P.; Gerard, I.; Hildebrandt, T.; Causier, A.; Pelouard, J. L.; Dagher, G.; Jehl, Z.; Naghavi, N.; Voorwinden, G.; Dimmler, B.; Powalla, M.; Guillemoles, J. F.; Lincot, D.; Etcheberry, A. Thinning of Cigs Solar Cells: Part I: Chemical Processing in Acidic Bromine Solutions. *Thin Solid Films* **2011**, 519 (21), 7207–7211.

(56) Canava, B.; Guillemoles, J. F.; Vigneron, J.; Lincot, D.; Etcheberry, A. Chemical Elaboration of Well Defined Cu(In,Ga)Se2 Surfaces after Aqueous Oxidation Etching. *J. Phys. Chem. Solids* **2003**, 64 (9–10), 1791–1796.

(57) Ferry, V. E.; Verschuuren, M. A.; Li, H. B. B. T.; Schropp, R. E. I.; Atwater, H. A.; Polman, A. Improved Red-Response in Thin Film a-Si:H Solar Cells with Soft-Imprinted Plasmonic Back Reflectors. *Appl. Phys. Lett.* **2009**, 95 (18), 183503.

(58) Fairbrother, A.; Garcia-Hemme, E.; Izquierdo-Roca, V.; Fontane, X.; Pulgarin-Agudelo, F. A.; Vigil-Galan, O.; Perez-Rodriguez, A.; Saucedo, E. Development of a Selective Chemical Etch to Improve the Conversion Efficiency of Zn-Rich Cu2ZnSnS4 Solar Cells. *J. Am. Chem. Soc.* **2012**, 134 (19), 8018–8021.

(59) Meyer, J.; Khalandovsky, R.; Gorrn, P.; Kahn, A. Moo3 Films Spin-Coated from a Nanoparticle Suspension for Efficient Hole-Injection in Organic Electronics. *Adv. Mater.* **2011**, 23 (1), 70–73.

(60) Guo, Y. Z.; Robertson, J. Origin of the High Work Function and High Conductivity of MoO3. *Appl. Phys. Lett.* **2014**, 105 (22), 222110.

(61) Butler, K. T.; Crespo-Otero, R.; Buckeridge, J.; Scanlon, D. O.; Bovill, E.; Lidzey, D.; Walsh, A. Band Energy Control of Molybdenum Oxide by Surface Hydration. *Appl. Phys. Lett.* **2015**, 107 (23), 231605.

(62) Antunez, P. D.; Bishop, D. M.; Sardashti, K.; Gokmen, T.; Gershon, T. S.; Lee, Y. S.; Gunawan, O.; Mankad, R.; Singh, S.; Kummel, A. C.; McCandless, B. E.; Haight, R. Open Circuit Voltage Improvements in CZTSSe Devices through High Work Function Back Contacts. Presented at the MRS Fall Meeting, Boston, MA, 2015.

(63) Greiner, M. T.; Helander, M. G.; Tang, W. M.; Wang, Z. B.; Qiu, J.; Lu, Z. H. Universal Energy-Level Alignment of Molecules on Metal Oxides. *Nat. Mater.* **2012**, 11 (1), 76–81.

(64) Battaglia, C.; Yin, X. T.; Zheng, M.; Sharp, I. D.; Chen, T.; McDonnell, S.; Azcatl, A.; Carraro, C.; Ma, B. W.; Maboudian, R.; Wallace, R. M.; Javey, A. Hole Selective MoOx Contact for Silicon Solar Cells. *Nano Lett.* **2014**, 14 (2), 967–971.